Predicting and Synthesizing Interface Stabilized 2D-Layers

Danielle M. Hamann,[†] Sven P. Rudin,[‡,¶] Tomoya Asaba,[‡] Filip Ronning,[‡,¶] Dmitri Leo M. Cordova,[†] Ping Lu,[§] David C. Johnson[†,*]

[†] Department of Chemistry and Materials Science Institute, University of Oregon, 1253 University of Oregon, Eugene, Oregon 97403 USA.

[‡] Los Alamos National Laboratory, Los Alamos, New Mexico, 87545, USA

[¶] Institute for Materials Science, Los Alamos, New Mexico, 87545, USA

[§] Sandia National Laboratories, Albuquerque, New Mexico, 87185, USA

Supporting Information Placeholder

ABSTRACT: The compound $(Pb_2MnSe_3)_{0.6}VSe_2$ was predicted to be kinetically stable based on DFT calculations on an island of Pb_2MnSe_3 between layers of VSe_2. This approach provides a high degree of freedom by not forcing interlayer lattice match, making it ideal to investigate the likelihood of formation of new incommensurate layer misfit structures. The free space around the island is critical, as it allow atoms to diffuse and hence exploring the local energy landscape around the initial configuration. $(Pb_2MnSe_3)_{0.6}VSe_2$ was synthesized via a near diffusionless reaction from precursors where a repeating sequence of elemental layers match the local composition and layer sequence of the predicted compound. The VSe_2 layer consists of a Se-V-Se trialyer with octahedral coordination of the V atoms. The Pb_2MnSe_3 layer consists of three rock salt like planes, with a MnSe layer between planes of PbSe. The center MnSe plane stabilizes the puckering of the outer PbSe layers. Electrical properties indicate that $(Pb_2Mn_1Se_3)_{0.6}VSe_2$ undergoes a charge density wave transition at ~100K and orders ferromagnetically at 35K. The combination of theory and experiment enables a faster convergence to new heterostructures than either approach in isolation.

The properties of interfaces and the structures that form at them – interfacial phases – are critically important in many technologies including solar cells, batteries, magnetic recording media, catalysts and integrated circuits. In addition to either kinetic or thermodynamic stability of the interface, diverse properties are needed to optimize performance in different applications. In solid state batteries, for example, an interface layer is desired on the metal anode that prevents metal dendrite growth, has high metal cation conductance and is electrically insulating.[1] In solar cells, one desires an interface that promotes charge separation and transport without any charge recombination sites.[2] In magnetic materials, interfaces modify, control, enhance, create and/or eliminate magnetic order depending on their properties.[3] In all these cases the properties depend on the electronic structure, chemical composition and structure of the interfacial phases, which can differ from known bulk compounds and often depend intimately on processing parameters.

Predicting and controlling the structure and composition of interfaces, particularly compositions and/or structures not found in bulk phase diagrams, remains an elusive goal. While some interface structures have been produced by design, for example HfO_x high K dielectrics[4] and the beautiful abrupt interfaces grown by molecular beam epitaxy (MBE),[5] most interface structures are made serendipitously, merely a consequence of processing conditions when different materials are placed in contact with one another. The evolution of an interface as a function of processing conditions (temperature, time, etc.) typically is alternatively limited by interdiffusion and nucleation, and the sequence of phase formation cannot be predicted.[6] Even during MBE growth, unexpected interfacial compounds can form that are not expected either from the relevant phase diagrams or from the growth conditions.[7] The termination of structures at interfaces creates unusual coordination environments and structural distortions as surface and volume free energies become comparable in magnitude. Consequently, most interfacial compounds are discovered serendipitously, often due to their impact on device properties, and optimized using trial and error approaches. While the structure and properties of discovered interface compounds are rationalized post discovery by theory, there is no approach developed to predict the many potential interfacial layers not present in bulk phase diagrams that may have desirable properties.

The past decade has seen the rapid growth of computational materials by design, combining data mining and advanced thermodynamic and electronic-structure methods that are enabled by advanced

computational resources.[8-11] These approaches search for new compositions and structures that are close to or below the convex hull of free energies calculated from combinations of known compounds[12] or calculated for an amorphous solid with the same composition.[13-14] The approaches range from substitutions of different elements into known structures[15] to evolutionary algorithms that explore the free energy landscape, capable of predicting new structure types.[16-18] These proposed new compounds create challenges for synthetic chemists, as many cannot be prepared using traditional synthetic methods due to the lack of kinetic control or because the compounds are not thermodynamically stable under the synthesis conditions.[19] The next step beyond computational "materials by design" (what to make) is to probe "reactions by design" (how to make) using both computation and experiment.

Here we present a theoretical approach to predict the kinetic stability of finite thickness interfacial layers that also probes the likelihood that it can be prepared. The computational procedure and the synthesis approach used in our study both explore local regions of the energy landscape around similar initial configurations. The computational approach probes if an initial nucleus of a particular structure is kinetically stable, and hence able to grow. The designed precursors used in the synthesis approach contain regions of appropriate composition for the nucleation of the targeted structures. We demonstrate the potential power of this collaborative approach through our investigation of the Mn-Pb-Se-V quaternary space searching for potential 2D magnetic layers. We predicted and synthesized a new hetereostructure containing a magnetic PbSe-MnSe-PbSe trilayer stable between VSe_2 layers.

The Mn-Pb-Se-V system was chosen because there is only one known thermodynamically stable ternary compound $[(PbSe)_{1+d}]_1[VSe_2]_1$ and no known quarternary compounds (see Figure 1).[22] There are also several known ternary compounds, $[(PbSe)_{1+d}]_m[VSe_2]_n$,[20, 21] providing a first test of our theoretical search approachThe known binary compounds (PbSe, MnSe, $MnSe_2$, VSe, VSe_2, V_2Se_9, V_5Se_8, V_3Se_4, V_5Se_4, VMn and VMn_4) provide a number of candidates as potential interfacial layers in other heterostructures. We focused our initial investigation on the VSe_2-MnSe-PbSe slice of the quaternary phase space, searching for heterostructures containing magnetic

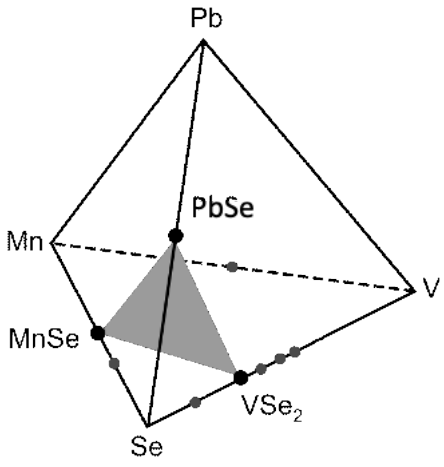

interfacial layers. VSe_2 is a layered compound containing octahedrally coordinated V between Se layers and is isostructural with CdI_2.[23] MnSe and PbSe are isostructural with NaCl at room temperature[24, 25] and a metastable zinc blend polymorph of MnSe has also been

Figure 1. The quaternary Mn-Pb-Se-V phase space showing the VSe_2-MnSe-PbSe plane investigated in this study. The black circles mark the compositions of the known binary compounds. Only VSe_2, MnSe, and PbSe are labeled.

synthesized.[26, 27] Both MnSe polymorphs magnetically order. Cubic MnSe is an antiferromagnet ordering at 140 K.[28] The hexagonal MnSe phase orders antiferromagnetically at ~250 K.[28]

METHODS

Our computational search approach focuses on the kinetic stability of potential interface phases, which are tested by independent structural optimizations using density functional theory (DFT) calculations.[29] Potential interfacial phases with various stoichiometries and crystal structures are constructed as an island between layers of adjacent layers (details in the SI). The free space around the islands allows atoms to move into more favorable configurations, lower the free energy, exploring the local energy landscape. This "island approximation" has been shown to successfully describe known incommensurate heterostructures.[30] Figure 2 shows the two general outcomes of the optimization step: the atoms in the island move either toward a recognizable, periodic pattern or toward an arrangement without forming such a pattern. The control of the optimization depends on finding an island size small enough to give a wide extent of the exploration, but not too small where the surface states dominate the pattern formed. The optimization aims

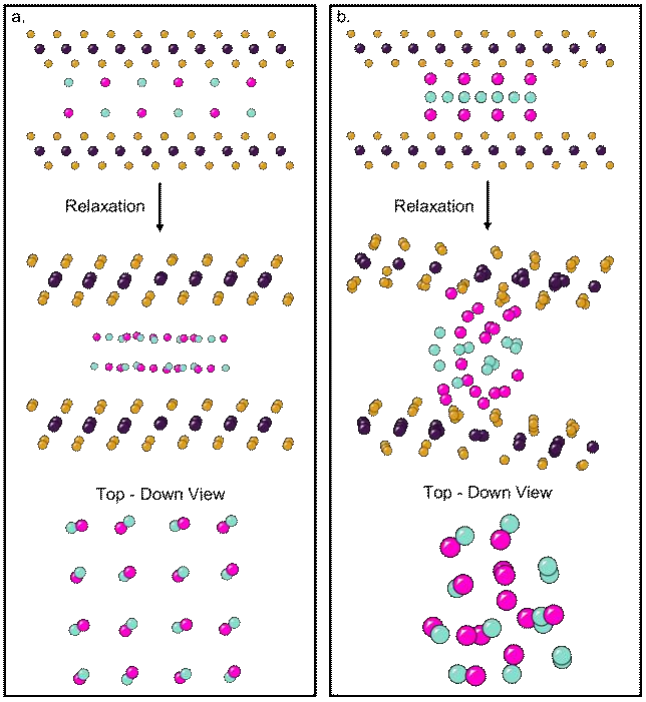

solely to test one property of the potential interface phase:

kinetic stability of a potential nuclei that would favor the nucleation and growth of the targeted structure.

Figure 2. A schematic of the theoretical approach used to examine the kinetic stability of constituent compound candidates. A candidate model structure of an AB compound with a rock salt structure that remains intact when relaxed (a). Both the side and top-down view of the promising system after relaxation contain a recognizable structure with systematic distortions due to the adjacent layers. The (b) panel contains a candidate model structure of an AB_2 compound which evolves into an amorphous fragment without long-range ordering when allowed to relax.

Optimized interface phases with islands in a recognizable, periodic pattern become candidates for synthesis.

Figure 3 shows the two critical advantages of representing one constituent layer as an island surrounded by vacuum between continuous slabs of the other constituent (as opposed to a complete layer under the same conditions). First, the atoms in the island can move and rearrange more easily on the edges of the island, potentially with substantial changes to the bonding. For the precursor in Fig. 2a, the optimization changes the Se atoms' initial bonding with four Mn to a bonding with three Mn (Fig. 2b). Second, the continuous layer of the second constituent fully determines the planar dimensions of the unit cell. This circumvents the need to construct a unit cell commensurate with the potential constituent layer, which *a priori* has unknown dimensions and orientation and may be incommensurate with the second constituent's dimensions. The smaller number of atoms also accelerates the calculation.

The theoretical predictions, presented below, were tested using precursors with local compositions and nanoarchitecture that mimic the targeted structures to favor their formation through near diffusionless transformations.[31-33] The precursors consist of repeated sequences of elemental layers deposited on a nominally room temperature silicon wafer that match the proposed composition of the interfacial phase and the composition of the adjacent layers. The synthesis accomplishes the local

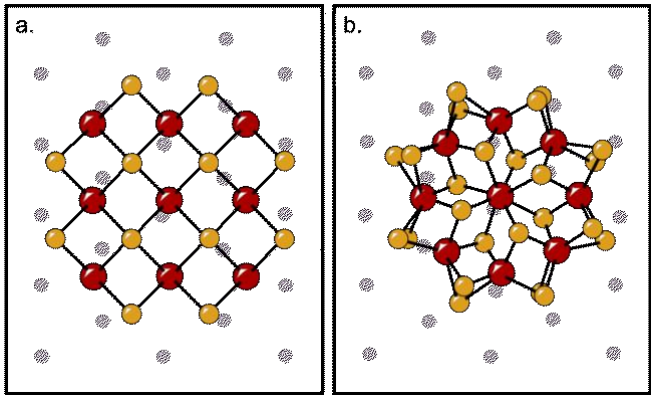

exploration of free energy space by controlling the extent of atomic diffusion via annealing temperature and time. A successful synthesis depends on finding an annealing temperature high enough for attaining the kinetically stabilized interface phase, but not so high that the precursor segregates into thermodynamically stable compounds.[34]

RESULTS AND DISCUSSION

Ultra-thin layers of Pb, V, Se and Mn were deposited in designed sequences to mimic the local compositions and nanoarchitecture of the targeted products. Precursors to $[PbSe]_{1.1}VSe_2$ were prepared with Pb|Se|V|Se layer sequences containing the correct number of atoms in the Pb|Se layer to form a rock salt structured PbSe bilayer and the correct number of atoms in the V|Se layer to form a

Figure 3. An example of a nine Mn (red) and 24 Se (yellow) island structure sandwiched between VSe_2 layers (only V shown in purple), which dramatically changes its structure while being relaxed. (a) is the initial structure and (b) is the structure after optimization.

VSe_2 trilayer. The layer sequence was repeated to obtain a total film thicknesses of ~50 nm. The precursors for $(Pb_2MnSe_3)_{0.6}VSe_2$, had a V|Se|Pb|Se|Mn|Se|Pb|Se layer sequence. In these precursors, the Pb|Se layers contained the correct number of atoms to form PbSe monolayers, the Mn|Se layer contained the number of atoms required to form a rock salt structured monolayer with the PbSe lattice parameters, and the V|Se layer contained the correct number of atoms to form a VSe_2 trilayer. This layer sequence was repeated to form films with a total film thickness of ~50 nm. Quartz crystal monitors were calibrated by measuring the amounts of each element in the resulting films using x-ray fluorescence[35] and iteratively adjusting the amount of time shutters were kept open to obtain the desired amount of each element. Figure 4. shows the composition of samples made in the VSe_2-MnSe-PbSe plane of the quaternary phase diagram.

The known $[PbSe]_{1.1}VSe_2$ heterostructure was used as a test of the computational approach. Computationally, an island of rock-salt structured PbSe was allowed to relax between continuous slabs of (001) trilayer slices of CdI_2-type structured VSe_2. The relaxed heterostructure for a bilayer of PbSe between VSe_2 approximates a fragment of a (001) bilayer slice of NaCl-type PbSe as found experimentally (see Figure 5a). PbSe islands of different

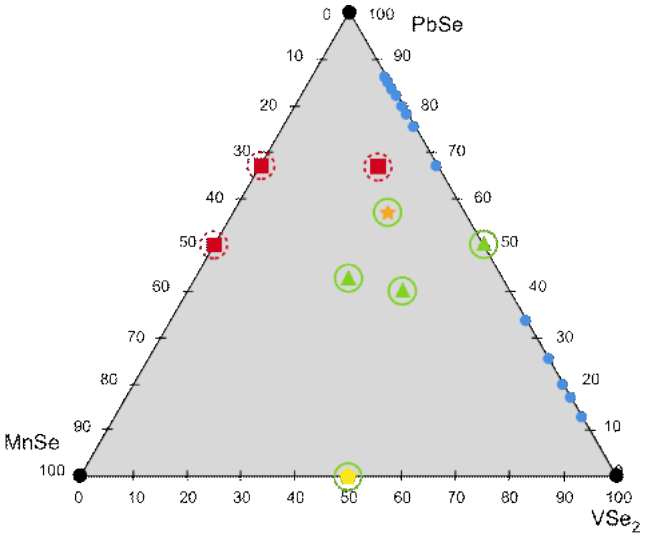

thicknesses and crystallographic orientations between VSe_2 layers also optimized into recognizable, periodic patterns of NaCl-type PbSe including fragments of a (001) monolayer, a (011) bilayer, and a (111) trilayer. Precursors mimicking the stable theoretical products were prepared. The Pb|Se|V|Se layer sequence targeting a bilayer of PbSe self-assembled into $[PbSe]_{1.1}VSe_2$ during low temperature annealing. The

Figure 4. Samples made in this study are marked in the VSe_2-MnSe-PbSe plane of the quaternary phase diagram. Circles indicate the results of the theoretical predictions. The solid symbols within the circles indicate the results of the calculations. Red indicates that no compound was stable at the predicted compositions. Green indicates that compounds were predicted to be local free energy minima and were successfully prepared. Yellow and orange indicates the predicted compounds began to form from the precursors during annealing but decomposed before fully forming. The blue circles indicate other $[(PbSe)_{1.1}]_m[VSe_2]_n$ metastable compounds that have previously been prepared.

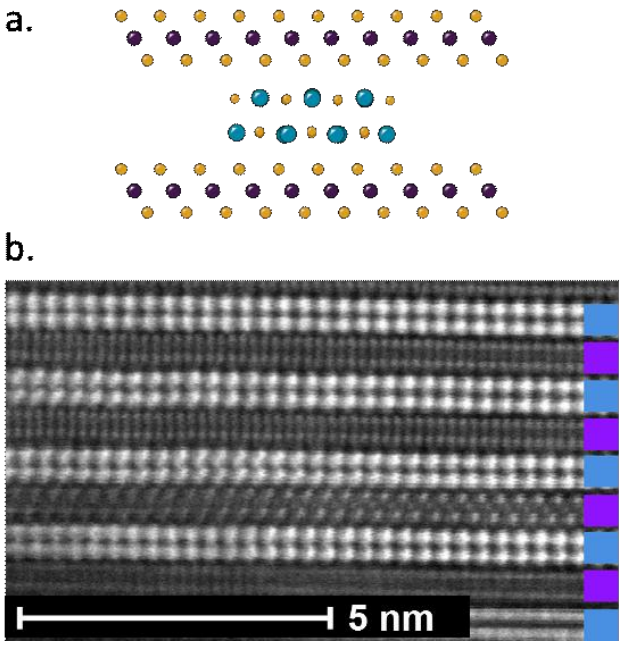

Figure 5. a. The optimized structure of an island of PbSe between VSe_2 layers. **b**. The HAADF-STEM image of a region of $[PbSe]_{1.1}VSe_2$ formed by annealing a designed precursor. The blue squares on the right identify PbSe layers and the purple squares align with VSe_2 layers.

HAADF-STEM cross-section image of $[PbSe]_{1.1}VSe_2$, Figure 5b, contains alternating layers of VSe_2 and bilayers of PbSe. All of the PbSe layers are being viewed down a [001] zone axis, but several different zone axes orientations are present for the VSe2 layers. While an area is shown with the layers orientated so many zone axes are present, in general there is rotational disorder in the stacking of the layers. It is not possible to form a monolayer or a trilayer of PbSe.[36]

Our computational and experimental results also diverged for MnSe-VSe_2 heterostructures. Several MnSe islands exhibited recognizable, periodic patterns when relaxed, including a fragment of a (001) trilayer slice of iron stannide-type structured MnSe and a (111) trilayer slice of NaCl-type structured MnSe. Annealing precursors with Mn|Se|V|Se layer sequences containing the correct number of atoms to form MnSe from the Mn|Se layers and VSe_2 from the V|Se layers at low temperatures (T < 250°C) results in an increase in the intensity of Bragg reflections due to the deposited layer sequence, which is consistent with self-assembly of a heterostructure (See Figure 6). Annealing above 250°C, however, resulted in the loss of the precursor layering and the formation of mixtures of the binary compounds.

Since the computational search show that both PbSe and MnSe favor similar NaCl-type structures between VSe_2 layers, we explored arrangements of PbSe-MnSe alloys between VSe_2 layers. Computationally, a NaCl-type structured PbSe-MnSe-PbSe trilayer island alternating with a complete CdI_2-type structured VSe_2 layer relaxes to the $(Pb_2MnSe_3)_{0.6}VSe_2$ heterostructure (Figure 7a). A precursor with a V|Se|Pb|Se|Mn|Se|Pb|Se sequence self-assembled.into this heterostructure during annealed at low temperatures (Figure 7b). Annealing the sample above 250 °C resulted in decomposition of the $(Pb_2MnSe_3)_{0.6}VSe_2$

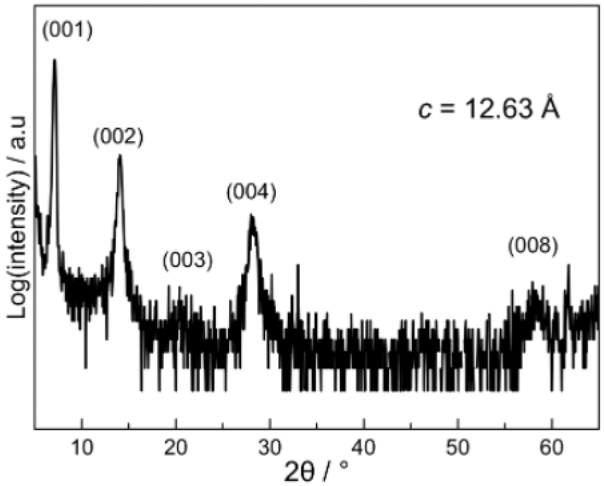

Figure 6. The specular diffraction pattern of an annealed precursor targeting a $(MnSe)_{1+x}VSe_2$ heterostructure. oo*l* Bragg reflections increase in intensity during low temperature annealing, consistent with a *c*-axis lattice parameter of 12.63Å.

heterostructure into a mixture of MnSe and a $[PbSe]_{1.1}VSe_2$ heterostructure.

The structure of the synthesized $(Pb_2MnSe_3)_{0.6}VSe_2$ heterostructure was determined using a combination of different experimental techniques. X-ray fluorescence (XRF) data collected on the annealed sample are consistent with the chemical formula $(Pb_2MnSe_3)_{0.6}VSe_2$. Specular diffraction data, shown in Fig. 8a, contain reflections that can all be indexed as oo*l* reflections. Rocking curve scans of the oo*l* reflections indicate that the $(Pb_2MnSe_3)_{0.6}VSe_2$ compound is crystallographically aligned with the *c*-axis perpendicular

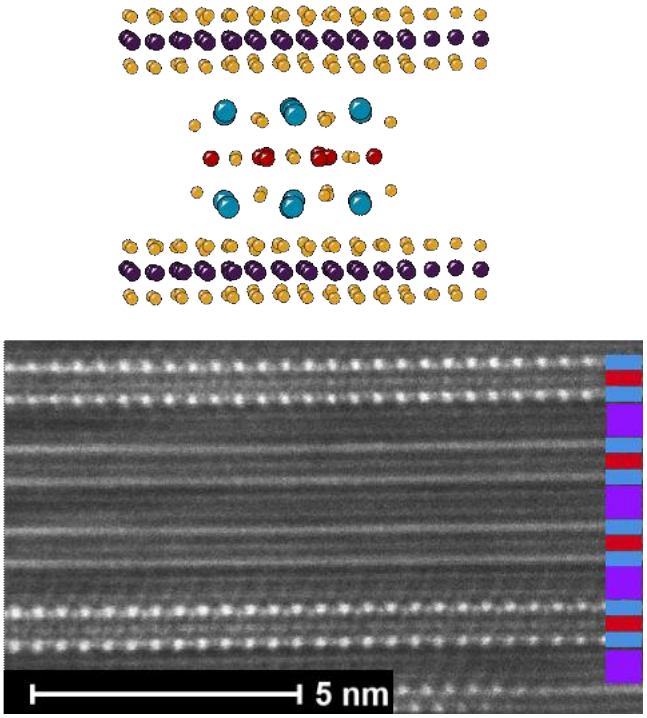

Figure 7. a. A schematic of the calculated island of the $(Pb_3Mn_2Se_5)_{1+\delta}VSe_2$ heterostructure. **b.** A representative HAADF STEM image of the $(Pb_2MnSe_3)_{0.6}VSe_2$ heterostructure.

to the substrate. The *c*-axis lattice parameter after annealing at 250 °C (14.96 Å) is consistent with that expected for the targeted $(Pb_2MnSe_3)_{0.6}VSe_2$ compound based on the expected constituent layers. In-plane diffraction data collected after annealing at 250 °C, (Fig. 8b) contains intensity maxima that can be indexed as *hk*o reflections coming from independent hexagonal and square lattices. The lattice parameter of the hexagonal phase (3.44 Å, computationally 3.46 Å) is close to that found for VSe_2 monolayers in $(PbSe)_{1.1})_mVSe_2$ compounds.[36] The lattice parameter of the square phase (5.99 Å, is close to that found for rock salt structured PbSe bilayers in $(PbSe)_{1.1}VSe_2$. An atomic-scale STEM energy dispersive x-ray spectroscopy (STEM-EDS) map of a representative area (Fig. 8c) shows that the structure consists of a VSe_2 layer on either side of a Pb_2MnSe_3 layer. The Pb_2MnSe_3 layer contains a MnSe middle layer with PbSe on either side. The changes in the EDS intensities for Mn, Pb, Se, and V through a single unit cell obtained by averaging over a region of the sample are shown in Fig. 8d The V intensity has a single maximum centered on the VSe_2 layer in the unit cell. The Pb intensity has two maxima corresponding to the outer two PbSe layers in the Pb_2MnSe_3 region of the structure. The Mn intensity has a single maximum centered between the Pb maxima in the Pb_2MnSe_3 layer. The Se intensity has two maxima on either side of the V maximum, corresponding to the two Se planes in VSe_2. The maxima for the Se in the Pb_2MnSe_3 layer are less distinct as the Se concentration is ~ half that found in the Se planes in VSe_2. The HAADF-STEM image of $(Pb_2MnSe_3)_{0.6}VSe_2$, shown in Fig. 7b, shows alternating layers of Pb_2MnSe_3 and VSe_2. There is rotational disorder from layer to layer, presumably due to independent nucleation events occurring in different layers as the precursor self assembles into $(Pb_2MnSe_3)_{0.6}VSe_2$. Two of the Pb_2MnSe_3 layers are orientated along the [110] zone axis, and the positions of the atomic columns are consistent with the Pb_2MnSe_3 layer having a distorted rock salt structure indicated by the in plane diffraction data. Along this zone axis, alternating columns of Pb and Se atoms are visible in the top and bottom of the Pb_2MnSe_3 layer. These PbSe layers are puckered, with the Se atoms displaced towards the MnSe layer and the Pb atoms pushed out from the central plane (computationally by 0.67 Å, on average). This results in the Mn cations in the center layer having four long bonds to Se within the Mn-Se plane and two shorter Mn-Se bond distances with the Se atoms in the Pb-Se plane. Columns of Se atoms can be observed, between the Pb columns in the upper and lower layers, displaced towards the center of the Pb_2MnSe_3 layer. The smaller size of the Mn atom relative to Pb enables the central Mn-Se layer to stabilize the puckering of the outer PbSe layer. Zone axis orientations of the VSe_2 layers are consistent with octahedral coordination of the central V layer by the adjacent Se layers. While the image shown contains no defects except for the turbostratic disorder of the stacking of the layers, the top and bottom of the samples typically contain regions with PbSe layers, presumably due to insufficient Mn in the precursor and/or reaction of Mn with advantageous oxygen during annealing. Presumably other defects, such as Mn on Pb sites or vice versa, were also formed during the self-assembly process.

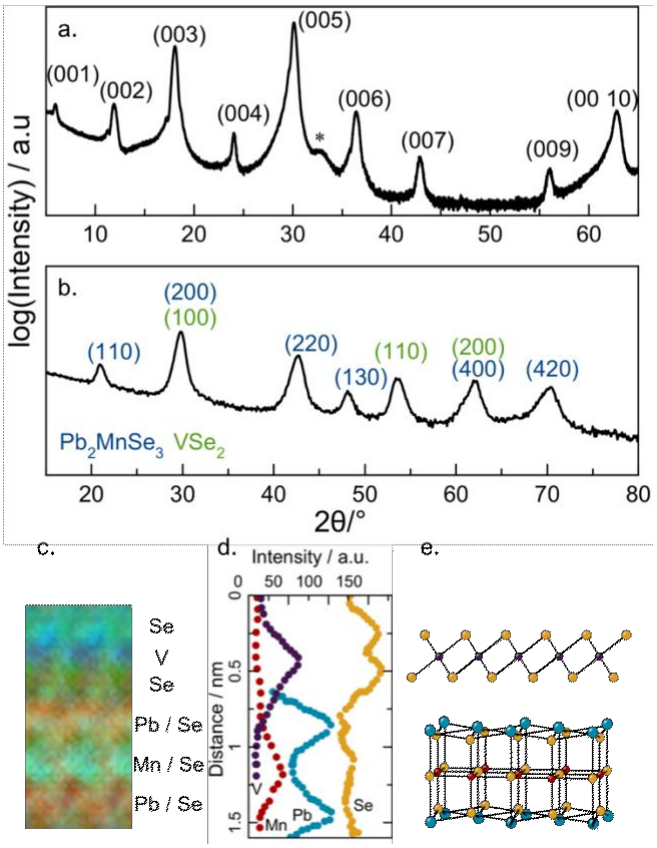

The calculated structure of $(Pb_2MnSe_3)_{0.6}VSe_2$, determined using a unit cell containing a complete layer of VSe_2 (25 unit cells) and a complete layer of Pb_2MnSe_3 (15 unit -

Figure 8. The specular diffraction pattern (a) contains only o*o*l reflections yielding a *c*-axis lattice parameter consistent with the $(Pb_2MnSe_3)_{0.6}VSe_2$ heterostructure. The reflections in the in-plane diffraction pattern (b) can be indexed to as *hk*o reflections for a hexagonal and a cubic unit cell and the lattice parameters correspond to those of the VSe_2 and Pb_2MnSe_3, layers, respectively. The STEM-EDS map (c) and intensity profile (d) indicate a V plane between planes of Se adjacent to a Pb/Se-Mn/Se-Pb/Se tri-layer. The structure determined from the STEM and diffraction data is schematically presented with Se atoms shown in yellow, V atoms in purple, Mn atoms in red and Pb atoms in blue (e).

cells), agrees well with the unit cell determined via a Le Bail refinement of the experimental diffraction data. The orientation between the two layers used to calculate the structural parameters rotated the layers by 15º relative to the optimized island structure to construct a computationally more tractable unit cell. The *c*-axis lattice parameter for the relaxed structure after the DFT structural optimization is slightly smaller than the experimental value (14.70 Å versus 14.96 Å). The calculated in-plane lattice parameter of the Pb_2MnSe_3 layer, 5.89 Å, is also slightly smaller than the experimental value (5.99Å).

The measured electrical transport properties of $(Pb_2MnSe_3)_{0.6}VSe_2$ and $(PbSe)_{1.1}VSe_2$ are shown in Figure 9. The resistivity of $(Pb_2MnSe_3)_{0.6}VSe_2$ decreases as temperature is decreased from room temperature, as expected for a metal, before increasing slowly as temperature is decreased below ~150K. The rate of increasing resistivity accelerates below ~100K. The upturn in resistivity at ~ 100K is similar to that found in $(PbSe)_{1.1}VSe_2$, although the magnitude of the increase is less and the transition is also less abrupt.[20, 37] The origin of the CDW in $(PbSe)_{1.1}VSe_2$ is from the VSe_2 monolayer. The signature upturn in resistivity remains if the thickness of the PbSe layer is increased[37] or if PbSe is replaced by SnSe to form the compounds $[(SnSe)_{1.1}]_mVSe_2$.[38,39] The temperature where the upturn occurs varies systematically with the thickness of the SnSe or PbSe layer.[37, 39] The sharpness of the upturn also varies, presumably as a result of changes in carrier concentration due to defects that form during self-assembly of the precursor.[40, ,41] The CDW found in the compounds with monolayers of VSe_2 is not present if the thickness of the VSe_2 is increased.[20, 42] The CDW is changed if modulation doping occurs[43] and is completely suppressed for large amounts of charge transfer, for example in $(BiSe)VSe_2$.[44] CDW transition in monolayers of VSe_2 have also been reported, and were shown to be sensitive to the heterointerface formed with the substrate.[45, 46] The rotational disorder present in both $(PbSe)_{1.1}VSe_2$ and $(Pb_2MnSe_3)_{0.6}VSe_2$ prevent direct measurement of the structural distortion caused by the localization of the conduction electrons.[40] A specific heat jump was reported at the CDW transition in $(SnSe)VSe_2$ due to the phase transition, which was used to estimate the density of electronic states removed by the formation of gaps at the Fermi surface.[40] The density of states removed is of the same order of magnitude as that reported for the transition in bulk $TiSe_2$. There is also a kink in the resistivity curve of $(Pb_2MnSe_3)_{0.6}VSe_2$ at around ~30 K, which is not present in $(PbSe)_{1.1}VSe_2$.

The Hall coefficient of $(Pb_2MnSe_3)_{0.6}VSe_2$ is positive and increases as temperature is decreased below ~100K. Both the sign and temperature dependence of the Hall coefficient are similar to that reported for $(PbSe)_{1.1}VSe_2$. The abrupt increase in the Hall coefficient of $(PbSe)_{1.1}VSe_2$ as temperature is de-creased below 100K is caused by the onset of a charge density wave (CDW),[20, 37] suggesting that a CDW also occurs in $(Pb_2MnSe_3)_{0.6}VSe_2$. Evidence for ferromagnetic ordering of the Mn orbital moments is found in the anomalous Hall effect observed in the field dependence of the Hall coefficient at low fields (figure 5). The Hall coefficient becomes non-linear below about ~ 30 K, which is the same temperature where we observe a kink in the resistivity curve. This anomalous Hall effect suggests that the sample is ferromagnetically ordered.[47] Further evidence for ferromagnetic behavior is observed in the hysteresis of the Hall resistivity verses field measurement shown in Fig S1.

The similarities in the magnitudes and temperature dependences of both the resistivity and Hall coefficient between $(PbSe)_{1.1}VSe_2$ suggest that $(Pb_2MnSe_3)_{0.6}VSe_2$ has a CDW, that Mn is divalent in the Pb_2MnSe_3 layer and that the extent of charge transfer and bonding between the Pb_2MnSe_3 layer and VSe_2 is similar to that found for the PbSe layer in $([PbSe)_{1.1}VSe_2$. The higher room temperature

resistivity of $(Pb_2MnSe_3)_{0.6}VSe_2$ relative to $(PbSe)_{1.1}VSe_2$ at room temperature is a consequence of the conducting VSe_2 layer being a smaller percentage of the total thickness of the unit cell. The similar CDW onset temperatures for $(Pb_2MnSe_3)_{0.6}VSe_2$ and $(PbSe)_{1.1}VSe_2$ is consistent with prior reports showing that the onset temperature does not change as the thickness of PbSe is varied in $([PbSe]_{1+\delta})_mVSe_2$ heterostructures.[25] It is important to note that the electrical properties reported here for $(Pb_2MnSe_3)_{0.6}VSe_2$ are distinctly different than that reported for bulk VSe_2, which has a negative Hall coefficient and only a small change in slope

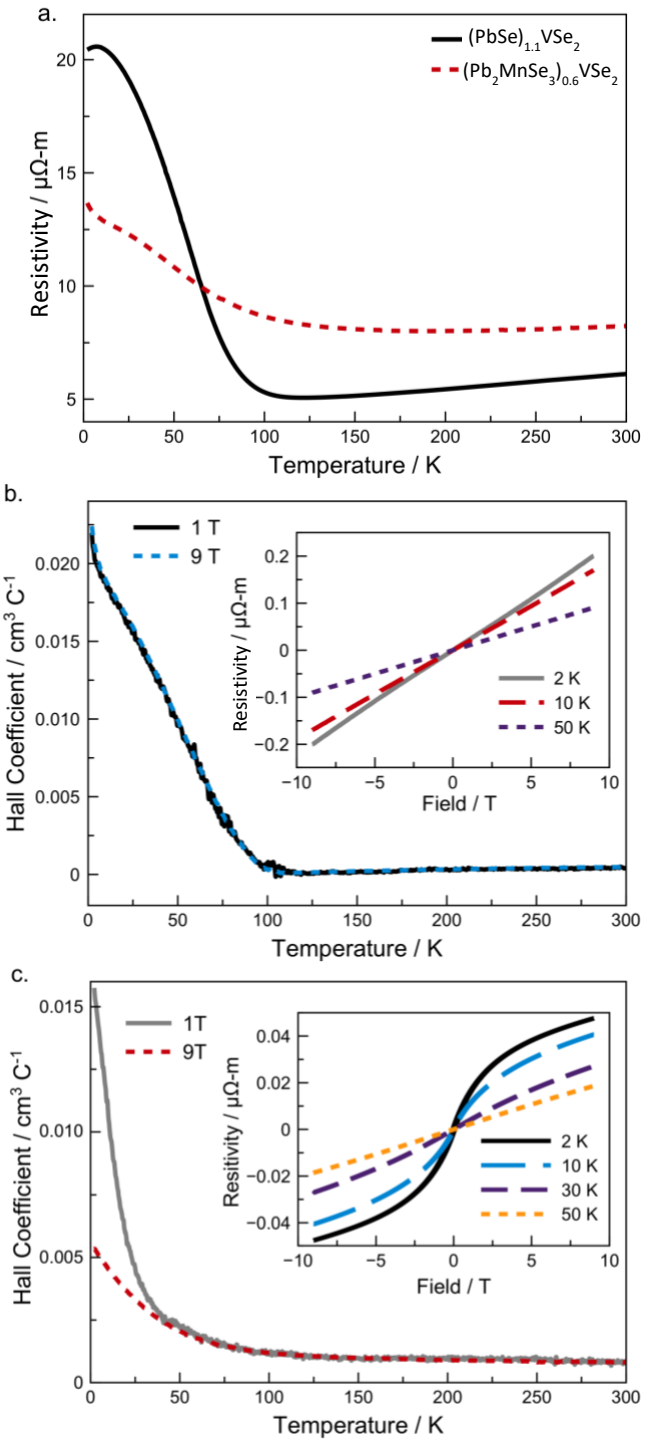

Figure 9. (a.) Resistivity versus temperature measured for $(Pb_2MnSe_3)_{0.6}VSe_2$ and $(PbSe)_{1.1}VSe_2$ heterostructures. (b.) Hall coefficient measured at two different magnetic fields as a function of temperature for $(PbSe)_{1.1}VSe_2$. Inset shows the field dependence of the Hall resistivity as a function of field. (c.) The Hall coefficient measured at two different fields as a function of temperature for $(Pb_2MnSe_3)_{0.6}VSe_2$. Inset shows the change in the field dependence of the Hall resistivity as a function of field.

as temperature is varied through its CDW transition.[48 - 50]

Properties of $(Pb_2MnSe_3)_{0.6}VSe_2$ were calculated using the relaxed supercell. The calculations indicate that it should be a ferromagnetic metal, agreeing with the transport measurements. The electronic density of states (DOS) at the Fermi level is contributed mainly by the V atoms and the magnetic moment is primarily from the Mn atoms. Bader analysis of the total spin density in the DFT calculations attributes around 4 μ_B to each Mn atom. Mn^{2+} has 5 electrons in the 3d orbitals and in a high spin D_{4h} local environment a magnetic moment of 5.9μ_B is expected for Mn^{2+}.[24] The smaller magnetic moment may be a consequence of charge transfer from the Pb_2MnSe_3 layer to VSe_2. A CDW is not seen in the relaxed unit cell from the DFT calculations, likely because the cell used was too small.

Calculations and synthesis attempts were also conducted on homologous interfacial compounds with thicker interfacial layers and with other first row transition metals besides Mn. Similarly, a heterostructure that extends the trilayer to a PbSe-MnSe-PbSe-MnSe-PbSe pentalayer island retains its structure upon optimization. A precursor with a Pb|Se|Mn|Se|Pb|Se|Mn|Se| Pb|Se stacking sequence results in diffraction patterns consistent with the proposed structure. Annealing a precursor with a Pb|Se|Pb|Se|Mn|Se|Pb|Se|Pb|Se stacking sequence resulted in the Mn diffusing to the next to layers adjacent to the outer PbSe layers, consistent with the MnSe layer stabilizing the surface distortion of the outer PbSe layer. We speculate that the thickness of the interior PbSe layer can be increased. NaCl-type structured PbSe-*T*Se-PbSe trilayer islands alternating with a complete CdI_2-type structured VSe_2 also are computationally stable when relaxed for T = Co, Cr, Fe, Ni, and Zn. This suggests that an entire family of prospective new materials, isostructural $(Pb_2TSe_3)_{1+\delta}VSe_2$ heterostructures, can be prepared. It may also be possible to change the identity of the dichalcogenide layer from V to other transition metals, as structurally analogous sulfide compounds are known.[51, 52]

CONCLUSIONS

A new heterostructure, $(Pb_2MnSe_3)_{0.6}VSe_2$, was predicted to be kinetically stable and was synthesized via a near diffusionless self-assembly from a designed precursor. Transport data indicates a charge density wave transition occurs at ~100K and that a transition to a ferromagnetic state occurs at 35K. The computational search approach used in this investigation finds kinetically stable, short-range, in-plane ordered arrangements of atoms, testing the stability of a nucleus of a phase between two interfaces.

The synthesis method uses local composition in a designed precursor to favor nucleation of specific structures and the nanoarchitecture of the precursor to favor the formation of specific stacking sequences and constituent layer thicknesses. The combination of theory and experiment enables a faster convergence to new heterostructures than either approach in isolation. Theory can quickly explore the stability of different structures and compositions and the number of simultaneous optimizations limited only by computational resources. The synthesis method can rapidly test systems predicted to be stable and can easily determine if heterostructures with thicker constituent layers and more complex stacking arrangements can be prepared.

The agreement between computational search and synthesis is not perfect. All successfully synthesized materials tested to date are computationally stable as the structures are relaxed. Those compounds predicted to be unstable have not been successfully synthesized. Not all computationally predicted stable materials, however, are successfully synthesized using designed precursors. A theoretically stable heterostructure can only be synthesized if the necessary annealing conditions (temperature, time, partial pressure of Se, ...) exists to convert the precursor to the targeted heterostructure without segregation to the thermodynamically stable mixture of binary compounds.

EXPERIMENTAL METHODS

Ultra-thin layers of different elements were deposited in high vacuum using either effusion cells (Se) of electron beam guns (Pb, V, Mn). The layer sequences were designed to mimic the desired product. Precursors to $[PbSe]_{1.1}VSe_2$ were prepared with a Pb|Se|V|Se layer sequence. The Pb|Se layer contained the correct number of atoms to form a rock salt structured PbSe bilayer. The V|Se layer contained the correct number of atoms in the to form a VSe_2 trilayer. The layer sequence was repeated to obtain a total film thickness of ~50 nm. To prepare a precursor for $(Pb_2MnSe_3)_{0.6}VSe_2$, a V|Se|Pb|Se|Mn|Se|Pb|Se sequence was prepared. In this precursor, the Pb|Se layers contained the correct number of atoms to form PbSe monolayers, the Mn|Se layer contained the number of atoms required to form a rock salt structured monolayer with the PbSe lattice parameters, and the V|Se layer contained the correct number of atoms to form a VSe_2 trilayer. This layer sequence was repeated to form films with a total film thickness of ~50 nm.

Samples were stored in a nitrogen glove box (>0.2 ppm oxygen) immediately after being taken out of the deposition chamber. Samples were annealed on a calibrated hot plate, which was preheated to the desired temperatures. The samples were placed face up on the hot plate for 15 minutes. After diffraction data was taken on the sample, it was reannealed at the next higher temperature. Samples were temporarily removed from the nitrogen atmosphere as needed for characterization.

Specular (00*l*) X-ray diffraction (XRD) and X-ray reflectivity (XRR) patterns were collected on a Bruker D8 diffractometer with Cu Kα radiation in θ-2θ locked-coupled scan mode. Each sample as aligned to the center of the goniometer before each scan. XRR patterns were collected from 0-11° to measure the total thickness of each film. Film thicknesses were determined using a linear-least-squares fit of the positions of Kiessig fringes using Braggs law corrected for refraction: $\sin^2(\theta) = n^2(\lambda^2/4d^2) + \sin^2(\theta_{crit})$, where d is the thickness of the entire film and θ_{crit} is the critical angle.

Grazing incidence XRD (GIXRD) and in-plane diffraction patterns were collected on a Rigaku Smartlab diffractometer with Cu Kα radiation and parallel-beam/parallel slit analyzer (PB/PSA) and parallel beam (PB) optics, respectively. Grazing incident scans were collected over a 2θ range of 5-65° with a step-size of 0.04°. In-plane diffraction patterns wer collected over a 2θ range of 15-110° with a step-size of 0.1°. An incident angle (ω) offset of 0.5° was used for both types of scans.

The number of atoms per unit area in each film was determined using a previously described X-ray fluorescence (XRF) technique.[22] The calibration curve for each element was created by preparing the most Se rich stoichiometric binary compound and using the Se calibration to determine the number of atoms per unit area in films with varying thickness. The relative error in atoms per unit area was determined by adding the relative errors of the calibration slope and of the XRF standard in quadrature, giving a relative error of ~2 % for the number of atoms/Å^2 of each element.

Cross-sections of two samples were prepared with an FEI Helios NanoLab 600i DualBeam FIB-SEM using standard lift-out procedures. High angle annular dark field (HAADF) images were collected on an FEI Titan G2 80-200 scanning transmission electron microscope (STEM) with a Cs probe corrector and ChemiSTEM technology (X-FEG and SuperX EDS with four windowless silicon drift detectors) operated at 200 kV.

ASSOCIATED CONTENT

Supporting Information. Details of calculations for depositions of initial precursors; Details of experimental methods; Hall resistivity verses field data. This material is available free of charge via the Internet at http://pubs.acs.org.

AUTHOR INFORMATION

Corresponding Author

* davej@uoregon.edu

Author Contributions

The manuscript was written through contributions of all authors.

Funding Sources

This research was supported by the following grants:
NSF DMR - 1905185
NSF DGE – 1309047
DOE Contract No. 89233218CNA000001 and NQI0001

Notes

The authors declare no competing financial interest.
All data required for evaluation of the conclusions in the paper are present in the main body of the paper and/or in the Supporting Information. Additional data related to this paper may be requested from the authors.

ACKNOWLEDGMENT

DMH acknowledges support from the National Science Foundation Graduate Research Fellowship Program under Grant No. 1309047. Any opinions, findings, and conclusions or recommendations expressed in this material are those of the author(s) and do not necessarily reflect the views of the National Science Foundation. The authors acknowledge support from the National Science Foundation under grant DMR-1905185. The authors acknowledge the Center for Advanced Materials Characterization in Oregon at the University of Oregon. SPR was supported by the US Department of Energy through the Los Alamos National Laboratory operated by Triad National Security, LLC, for the National Nuclear Security Administration of U.S. Department of Energy (Contract No. 89233218CNA000001), with funding from the New Mexico Small Business Assistance Program through the Laboratory Partnership with Small Business Tax Credit Act. SPR expresses deep gratitude to G. Scantlen and team at CreativeC for numerous motivating discussions and for the use of their VASP Instrument prototype computational platform, without which the more demanding calculations would not have been possible. TA acknowledges support from the LANL Directors Postdoctoral Funding LDRD program. F.R. is supported by the U.S. Department of Energy, Office of Science, National Quantum Information Science Research Centers, Quantum Science Center grant number NQI0001. This work was performed, in part, at the Center for Integrated Nanotechnologies, an Office of Science User Facility operated for the U.S. Department of Energy (DOE) Office of Science by Los Alamos National Laboratory (Contract DE-AC52-06NA25396) and Sandia National Laboratories (Contract DE-NA-0003525). This paper describes objective technical results and analysis. Any subjective views or opinions that might be expressed in the paper do not necessarily represent the views of the U.S. Department of Energy or the United States Government.

ABBREVIATIONS

DFT, Density-functional theory; MBE, Molecular beam epitaxy; 2D, two dimensional; HAADF STEM, high-angle annular dark-field scanning transmission electron microscopy; XRF, X-ray fluorescence; STEM-EDS, scanning transmission electron microscopy energy dispersive x-ray spectroscopy; CDW, charge density wave; DOS, density of states; XRD, X-ray diffraction; XRR, X-ray reflectivity; GIXRD, Grazing incidence X-ray diffraction.

REFERENCES

(1) Xu, L.; Tang, S.; Cheng, Y.; Wang, K.: Liang, J.; Liu, C.; Cao, Y.; Wei, F.; Mai, L. Interfaces in Solid-State Lithium Batteries, *Joule* **2018**, 2, 1991-2015.

(2) Weinhardt, L.; Hauschild, D.; Heske, C. Surface and Interface Properties in Thin-Film Solar Cells: Using Soft X-rays and Electrons to Unravel the Electronic and Chemical Structure, *Adv Mater.* **2019**, 31, 1806660.

(3) Hellman, F.; Hoffmann, A.; Tserkovnyak, Y.; Beach, G. S. D.; Fullerton, E. E.; Leighton, C.; MacDonald, A. H.; Ralph, D. C.; Arena, D. A.; Dürr, H. A.; Fischer, P.; Grollier, J.; Heremans, J. P.; Jungwirth, T.; Kimel, A. V.; Koopmans, B.; Krivorotov, I. N.; May, S. J.; Petford-Long, A. K.; Rondinelli, J. M.; Samarth, N.; Schuller, I. K.; Slavin, A. N.; Stiles, M. D.; Tchernyshyov, O.; Thiaville, A.; Zink, B. L. Interface-Induced Phenomena in Magnetism, *Rev. Mod. Phys.* **2017**, 89, 025006.

(4) Wilk, G. D.; Wallace, R. M.; Anthony, J. M. High-κ gate dielectrics: Current Status and Materials Properties Considerations, *J. Appl. Phys.* **2001**, 89, 5243-5275.

(5) Ohtomo, A.; Muller, D. A.; Grazul, J. L.; Hwang, H. Y. Artificial Charge-Modulation in Atomic-Scale Perovskite Titanate Superlattices, *Nature*, **2002**, 419, 378–380.

(6) Walser, R. M.; Bené, R. W. First Phase Nucleation in Silicon–Transition-Metal Planar Interfaces, *Appl. Phys. Lett.*, **1976**, 28, 624-625.

(7) Wang, M.; Li, P.; Xu, J.; Liu, Z.; Ge, J.; Wang, G.; Yang, X.; Xu, Z.; Ji, S.; Gao, C. L.; Qian, D.; Luo, W.; Liu, C.; Jia, J. Interface Structure of a Topological Insulator/Superconductor Heterostructure, *New J. Phys.*, **2014**, 16, 123043.

(8) Curtarolo, S.; Hart, G. L. W.; Nardelli, M. B.; Mingo, N.; Sanvito, S.; Levy, O. The High-Throughput Highway to Computational Materials Design, *Nat. Mater.* **2013**, 12, 191-201.

(9) Jain, A.; Ong, S. P.; Hautier, G.; Chen, W.; Richards, W. D.; Dacek, S.; Cholia, S.; Gunter, D.; Skinner, D.; Ceder, G.; Persson, K. A. Commentary: The Materials Project: a Materials Genome Approach to Accelerating Materials Innovation, *APL Mater.* **2013**, 1, 011002.

(10) Pickard, C. J.; Needs, R. J. High-Pressure Phases of Silane, *Phys. Rev. Lett.* **2006**, 97, 045504.

(11) Oganov, A. R.; Lyakhov, A. O.; Valle, M. How Evolutionary Crystal Structure Prediction Works - and Why, *Acc. Chem. Res.* **2011**, 44, 227-237.

(12) Bartel, C. J.; Trewartha, A.; Wang, Q.; Dunn, A.; Jain, A.; Ceder, G. A Critical Examination of Compound Stability Predictions From Machine-Learned Formation Energies, *Npj Comput. Mater.* **2020**, 6, 97.

(13) Sun, W.; Dacek, S. T.; Ong, S. P.; Hautier, G.; Jain, A.; Richards, W. D.; Gamst, A. C.; Persson, K. A. The Thermodynamic Scale of Inorganic Crystalline Metastability, *Sci. Adv.*, **2016**, 2, e1600225.

(14) Aykol, M.; Dwaraknath, S. S.; Sun, W.; Persson, K. A. Thermodynamic Limit For Synthesis of Metastable Inorganic Materials, *Sci. Adv.* **2018**, 4, eaaq0148.

(15) Fredeman, D. J.; Tobash, P. H.; Torrez, M. A.; Thompson, J. D.; Bauer, E. D.; Ronning, F.; Tipton, W. W.; Rudin, S. P.; Hennig, R. G. Computationally Driven Experimental Discovery of the $CeIr_4In$ Compound, *Phys. Rev. B* **2011**, 83, 224102.

(16) Tipton, W. W.; Hennig, R. G. A Grand Canonical Genetic Algorithm for the Prediction of Multi-Component Phase Diagrams and Testing of Empirical Potentials, *J. Phys.: Condens. Matter* **2013**, 25, 495401.

(17) Oganov, A. R.; Glass, C. W. Crystal Structure Prediction Using ab Initio Evolutionary Techniques: Principles and Applications, *J. Chem. Phys.* **2006**, 124, 244704.

(18) Trimarchi, G.; Zunger, A. Global Space-Group Optimization Problem: Finding the Stablest Crystal Structure Without Constraints, *Phys. Rev. B* **2007**, 75, 104113.

(19) Narayan, A.; Bhutani, A.; Rubeck, S.; Eckstein, J. N.; Shoemaker, D. P.; Wagner, L. K. Computational and Experimental Investigation for New Transition Metal Selenides and Sulfides: The Importance of Experimental Verification for Stability, *Phys. Rev B* **2016**, 94, 045105.

(20) Hite, O. K.; Falmbigl, M.; Alemayehu, M. B.; Esters, M.; Wood, S. R.; Johnson, D. C. Charge Density Wave Transition in $(PbSe)_{1.11}(VSe_2)_n$ Heterostructures With n = 1, 2, and 3, *Chem. Mater.* **2017**, 29, 5646–5653.

(21) Cordova, D. L. M.; Kam, T. M.; Fender, S. S.; Tsai, Y. H.; Johnson, D. C. Strong Non-Epitaxial Interactions: Crystallographically Aligned PbSe on VSe_2, *Phys. Stat. Sol.*, **2019**, 1800896.

(22) Reisinger, G. R.; Richter, K. W . Phase Equilibria and New Misfit Layer Compound in the Ternary System of Pb–Se–V, *J. Alloys Compd.,* **2020**, 831, 154730.

(23) Feroze, A.; Na, H. R.; Park, Y. C.; Jun, J.; Jung, M.; Lee, J.; Kim, J.; Seong, M.; Hong, S.; Chun, S.; Lee, S. In-Depth Structural Characterization of 1T-VSe_2 Single Crystals Grown by Chemical Vapor Transport, *Cryst. Growth Des.*, **2020**, *20*, 2860–2865.

(24) Ramsdell, L. S. The Crystal Structure of Some Metallic Sulfides, *Am. Min.* **1925**, 9-10, 281-304.

(25) Schlesinger, M. E. The Mn-Se (Manganese-Selenium) System, *J. Phase Equilib.*, **1998**, 19, 588-590.

(26) Litvinov, D.; Gerthsen, D.; Rosenauer, A.; Daniel, B.; Hetterich, M. Sphalerite-Rock Salt Phase Transition in ZnMnSe Heterostructures, *Appl. Phys. Lett.*, **2004**, 85, 751-753.

(27) Ishibe, I.; Nabetani, Y.; Kato, T.; Matsumoto, T. MBE Growth and RHEED Characterization of MnSe/ZnSe Superlattices on GaAs (1 0 0) Substrates, *J. Cryst. Growth*, **2000**, 214, 172-177.

(28) Efrem D'Sa, J. B. C.; Bhobe, P. A.; Priolkar, K. R.; Das, A.; Krishna, P. S. R.; Sarode, P. R.; Prabhu, R. B. Low Temperature Magnetic Structure of MnSe, *Pramana*, **2004**, 63, 227-232.

(29) Rudin, S. P. A Density Functional Theory Calculations-Based Approach that Predicts Layered Materials with Emergent Structures, **2016**, arXiv:1611.07510 [cond-mat.mtrl-sci].

(30) Rudin, S. P. Johnson, D. C. Density Functional Theory Calculations of the Turbostratically Disordered Compound $[(SnSe)_{(1+y)}]_m(VSe_2)_n$, *Phys. Rev. B*, **2015**, 91, 144203.

(31) Johnson, D. C. Controlled Synthesis of New Compounds Using Modulated Elemental Reactants, *Curr. Opin. Solid State Mater. Sci.* **1998**, 3, 159–167.

(32) Cordova, D. L. M.; Johnson, D. C. Synthesis of Metastable Inorganic Solids with Extended Structures, *Chem. Phys. Chem.*, **2020**, 21, 1345-1368**.**

(33) Esters, M.; Alemayehu, M.; Jones, Z.; Nguyen, N. T.; Anderson, M. D.; Grosse, C.; Fischer, S.; Johnson, D. C. Synthesis of Inorganic Structural Isomers By Diffusion-Constrained Self-Assembly of Designed Precursors: A Novel Type of Isomerism, *Angew. Chem. Int. Ed.* **2015**, 54, 1130–1134.

(34) Gunning, N. S.; Feser, J.; Beekman, M.; Cahill, D. G.; Johnson, D. C. Synthesis and Thermal Properties of Solid-State Structural Isomers: Ordered Intergrowths of SnSe and $MoSe_2$, *J. Am. Chem. Soc.*, **2015**, 137, 8803–8809.

(35) Hamann, D. M.; Bardgett, D.; Cordova, D. L. M.; Maynard, L. A.; Hadland, E. C.; Lygo, A. C.; Wood, S. R.; Esters, M.; Johnson, D. C. Sub-Monolayer Determination of the Number of Atoms Per Unit Area in Ultrathin Films Using X-ray Fluorescence, *Chem. Mater.,* **2018**, 30, 6209–6216.

(36) Cordova, D. L. M.; Fender, S. S.; Hooshmand, M. S.; Buchanan, M. R.; Davis, J.; Kam, T. M.; Gannon, R. N.; Fischer, R.; Lu, P.; Hanken, B. E.; Asta, M.; Johnson D. C. The Instability of Monolayer Thick PbSe on VSe_2, *Chem. Mater.*, **2020,** 32**,** 7992–8003.

(37) Cordova, D. L. M.; Fender, S. S.; Kam, T. M.; Lu, P.; Fischer, R.; Johnson, D. C. Designed Synthesis and Structure-Property Relationships of Kinetically Stable $[(PbSe)_{1+\delta}]_m(VSe_2)_1$ (m = 1, 2, 3, 4) Heterostructures, *Chem. Mater.*, **2019**, 31, 8473-8483..

(38) R. Atkins, S. Disch, Z. Jones, I. Häeusler, C. Grosse, S. F. Fischer, W. Neumann, P. Zschack, D. C. Johnson, Synthesis, Structure and Electrical Properties of a New Tin Vanadium Selenide, *J. Solid State Chem.,* **2013**, *202,* 128-133.

(39) Atkins, R.; Dolgos, M.; Fiedler, A.; Grosse, C.; Fischer, S. F.; Rudin, S. P.; Johnson, D. C. Synthesis and Systematic Trends in Structure and Electrical Properties of $[(SnSe)_{1.15}]_m(VSe_2)_1$, m = 1, 2, 3, and 4, *Chem. Mater.* **2014**, 26, 2862–2872.

(40) Falmbigl, M.; Putzky, D.; Ditto, J.; Esters, M.; Bauers, S. R.; Ronning, F.; Johnson, D. C. Influence of Defects on the Charge Density Wave of $([SnSe]_{1+\delta})_1(VSe_2)_1$ Ferecrystals, *ACS Nano*, **2015**, 9, 8440–8448.

(41) Falmbigl, M.; Putzky, D.; Ditto, J.; Johnson, D. C. Influence of Interstitial V on Structure and Properties of Ferecrystalline $([SnSe]_{1.15})_1(V_{1+x}Se_2)_n$ for n = 1, 2, 3, 4, 5, and 6, *J. Sol. State Chem.* **2015**, 231, 101–107.

(42) Falmbigl, M.; Fiedler, A.; Atkins, R. E.; Fischer, S. F.; Johnson, D. C. Suppressing a Charge Density Wave by Changing Dimensionality in the Ferecrystalline Compounds $([SnSe]_{1.15})_1(VSe_2)_n$ with n = 1, 2, 3, 4., *Nano Lett.* **2015,** 15, 943-948.

(43) Falmbigl, M.; Hay, Z.; Ditto, J.; Mitchson, G.; Johnson, D. C. Modifying a Charge Density Wave Transition By Modulation Doping: Ferecrystalline Compounds $([Sn_{1-x}Bi_xSe]_{1.15})_1(VSe_2)_1$ with $0 \le x \le 0.66$, *J. Mater. Chem. C*, **2015**, 3, 12308-12315.

(44) Hite, O. K.; Nellist, M.; Ditto, J.; Falmbigl, M.; Johnson, D. C. Transport Properties of Vanadium Diselenide Monolayers Separated by Bilayers of BiSe, *J. Mater. Res.*, **2016**, 31, 886-892.

(45) Feng, J.; Biswas, D.; Rajan, A.; Watson, M. D.; Mazzola, F.; Clark, O. J.; Underwood, K.; Marković, I.; McLaren, M.; Hunter, A.; Burn, D. M.; Duffy, L. B.; Barua, S.; Balakrishnan, G.; Bertran, F.; Le Fevre, P.; Kim, T. K.; van der Laan, G.; Hesjedal, T.; Wahl, P.; King, P. D. C. Electronic Structure and Enhanced Charge-Density Wave Order of Monolayer VSe_2, Nano Lett. **2018,** 18, 4493–4499.

(46) Duvjir, G.; Choi, B. K.; Jang, I.; Ulstrup, S.; Kang, S.; Ly, T. T.; Kim, S.; Choi, Y. H.; Jozwiak, C.; Bostwick, A.; Rotenberg, E.; Park, J.; Sankar, R.; Kim, K.; Kim, J.; Chang, Y. J. Emergence of a Metal–Insulator Transition and High-Temperature Charge-Density Waves in VSe_2 at the Monolayer Limit ,Nano Lett. **2018**, 18, 5432–5438.

(47) Nagaosa, N.; Sinova, J.; Onoda, S.; MacDonald, A. H.; Ong, N. P. Anomalous Hall Effect, *Rev. Mod. Phys.* **2010**, 82, 1539-1592.

(48) Bayard, M.; Sienko, M. J. Anomalous Electrical and Magnetic Properties of Vanadium Diselenide, *J. Solid State Chem.*, **1976**, 19, 325–329.

(49) van Bruggen, C. F.; Haas, C. Magnetic Susceptibility and Electrical Properties of VSe_2 Single Crystals, *Solid State Commun.*, **1976**, 20, 251–254.

(50) Thompson, A. H.; Silbernagel, B. G. Correlated Magnetic and Transport Properties in the Charge-Density-Wave States of VSe_2, Phys. Rev. B **1979**, 19, 3420–3426.

(51) Deudon, C.; Lafond, A.; Leynaud, O.; Moëlo, Y.; Meershaut, A. Crystal Structures and Magnetic Properties of the Two Misfit Layer Compounds: $[SrGd_{0.5}S_{1.5}]_{1.16}$ NbS_2 and $[Sr(Fe,Nb)_{0.5}S_{1.5}]_{1.13}$ NbS_2, *J. Solid State Chem.*, **2000**, *155*, 1-8.

(52) Lanfond, A.; Deudon, C.; Meershaut, A.; Palvadeau, P.; Moëlo, Y.; Briggs, A. Structure Determination and Physical Properties of the Misfit Layered Compound $(Pb_2FeS_3)_{0.58}NbS_2$, J. Solid State Chem., **1999**, 142, 461-469.

A new theoretical search procedure was used to predict that a rock salt structured 2D layer of Pb_2MnSe_3 would be stable between VSe_2 layers. It was successfully synthesized via a near diffusion less self-assembly from a designed precursor. $(Pb_2MnSe_3)_{0.6}VSe_2$ has a charge density wave transition and at lower temperatures becomes a ferromagnetic. This investigation illustrates that many 2D layers are possible that are not stable as bulk solids that can be predicted and synthesized.